MESO-SCALE PHASE FIELD MODELLING OF REINFORCED CONCRETE STRUCTURES SUBJECTED TO CORROSION OF MULTIPLE REINFORCEMENTS

Xiaofei Hu [1], Huiqian Xu[1], Xun Xi[2*], Peng Zhang[3] and Shangtong Yang[2]

1 State Key Laboratory of Structural Analysis for Industrial Equipment, International Research Center for Computational Mechanics, Dalian University of Technology, Dalian 116024, PR China

2 Department of Civil and Environmental Engineering, University of Strathclyde, Glasgow G1 1XJ, UK

3 Department of Civil and Environmental Engineering, The Hong Kong Polytechnic University, Hong Kong, China

Abstract

Corrosion-induced concrete cover cracking is one of major deterioration mechanisms for reinforced concrete (RC) structures. Concrete cracking caused by corrosion of multiple reinforcements at the meso-scale involves complex toughening mechanism, stress redistribution and crack interaction. It brings significant challenge to accurately predicting the cover cracking which, in most cases, represents a critical stage of serviceability. This paper aims to develop a meso-scale phase filed model for concrete cover cracking induced by corrosion of multiple reinforcements. Concrete is treated as a three-phase heterogeneous material, consisting of aggregates, mortar and interfacial transition zones (ITZ). The developed method is implemented into ABAQUS explicit regime through an in-house VUEL subroutine. The crack patterns and crack width development of concrete induced by corrosion are obtained. The model is also verified against experimental results on the crack width development and crack patterns. Further, a parametric study is carried out to investigate the effects of reinforcement spacing, cover thickness, ITZ fracture properties on concrete cover cracking. Some toughening mechanisms including crack deflection, aggregate/mortar bridging and crack bifurcation in concrete have been captured in the model. ITZ fracture properties significantly affects the crack pattern of concrete cover. The developed method enables high fidelity numerical models with up to tens of millions of degrees of freedom (DOFs), and the completed failure processes of concrete cover are well predicted.

Keywords: durability; phase field model; corrosion; crack pattern; multiple reinforcements.

This is a peer-reviewed, accepted author manuscript of the following article: Hu, X., Xu, H., Xi, X., Zhang, P., & Yang, S. (2022). Meso-scale phase field modelling of reinforced concrete structures subjected to corrosion of multiple reinforcements. Construction and Building Materials, 321, [126376]. https://doi.org/10.1016/j.conbuildmat.2022.126376

1. Introduction

Reinforced concrete (RC) structures are widely used in buildings, bridges, piers, tunnels and many other civil engineering applications. During the service life, however, RC structures are subjected to reinforcement corrosion, especially in the chloride-laden and/or carbon dioxide environment. Corrosion of reinforcement can cause spalling or delamination of concrete cover, reduce the bonding strength with concrete and hence decrease the load bearing capacity of the RC structures, bringing great threat to the durability and serviceability of the structures. For instance, it was reported that 70-90% of practical cases of premature deterioration of RC structures were dominated by reinforcement corrosion [1].

Considerable research has been carried out on the corrosion-induced concrete cracking problems of RC structures [2-9]. Bhargava et al. [10] developed an analytical model to predict the time for cover cracking by considering concrete cracking as a tension-softening process. Li et al. [5] proposed an analytical model to predict the corrosion-induced crack width of concrete based on fracture mechanics. Further, Li and Yang [6] derived a model accounting for the strength of cracked concrete using the concept of fracture energy and predicted the crack width development over time under the combined reinforcement corrosion and applied load. Zhang et al. [9] proposed an analytical model to predict the concrete cracking time in consideration of initial defects in concrete and found an initial defect around concrete surface was more destructive on corrosion-induced concrete cracking than an initial defect inside the concrete. The existing analytical models on predicting corrosion-induced concrete cracking have provided useful tools to assess the serviceability of corrosion-affected RC structures. However, almost all existing analytical models were focused on a single reinforcing bar due to extreme difficulties in addressing the interactions between stress fields and cracks of different reinforcements by analytical methods.

Within a RC structure, the single rebar corrosion problem or assumption can only provide insight in the localized cover failure; for the whole concrete cover performance under long-term service, the corrosion of multiple reinforcements in the RC structures will have to be considered. In fact, the corrosion of multiple reinforcing bars within the structure can result in different cracking patterns and failure modes as stress fields and cracks can obviously interact [11]. In such cases, numerical approaches bring distinct advantages. Zhang et al. [12] employed a finite element (FE) model to simulate concrete cracking induced by corrosion of two reinforcements and found delamination of cover was more prone to occur for RC structures with a smaller rebar spacing. Cui and Alipour [13] developed a three-dimensional FE model to investigate the concrete cover cracking induced by corrosion of three reinforcements and found more elements were damaged for a thinner concrete cover. Cheng et al. [14] developed a chemical-mechanical coupled model to simulate non-uniform corrosion of multiple reinforcements and concrete cracking, and found that, with the increase of cover thickness, the crack initiation time became longer. Among the above simulations, concrete damage plasticity models were employed to predict the crack patterns of RC beams induced by corrosion. However, corrosion-induced concrete cracking is a typical fracture type problem, i.e., tension-dominated. Therefore, it poses concerns on the accuracy and rationale by using the plasticity-based damage model. Chen et al. [15] developed a lattice model to simulate the crack patterns of concrete cover induced by uniform corrosion of two reinforcing bars. They found that an inner transverse crack connecting two reinforcing bars formed before concrete surface cracking for a small reinforcement spacing. Xi and Yang [16] developed a time-dependent corrosion model and simulated multiple reinforcement corrosion induced concrete cracking through inserting zero-thickness cohesive elements into the FE mesh. Although the lattice model and cohesive crack model can simulate complex concrete cracking problems, the crack propagations are inevitably dependent on the original mesh. Besides, the modelling capability of such methods is limited due to computational expenses and the iteration convergence issue. The computational models reported in the literatures usually have a few tens/hundreds of thousands of degrees of freedom (DOFs).

Moreover, most existing numerical models treated concrete as homogeneous when simulating the crack propagation induced by the corrosion of multiple reinforcements [11-16]. The homogeneity assumption can only yield an approximate response while concrete is in fact heterogeneous especially at the meso-scale, consisting of aggregates, mortar and interfacial transmission zones between aggregates and mortar (i.e., ITZ). Further, concrete cracking involves toughing mechanisms including micro cracks shielding, crack deflection, aggregate bridging, etc., and ITZ plays an important role in simulating the concrete cracking [17-20]. Thus, meso-scale modelling by considering the concrete as a multi-phase quasi-brittle material will provide rational insights in the cracking initiation and propagation in concrete. However, to model arbitrary cracking and crack interactions in concrete induced by corrosion of multiple reinforcements at the meso-scale, a computational model with high fidelity could result in ten million DOFs or more, which has posed a nearly impossible challenge to the existing numerical methods.

In the recent years, a phase field model for fracture has been developed and become popular in the community of computational mechanics [21]. The model utilizes crack regularization and the Frankfort-Marigo variational principle [22] to form a non-local damage model, thus has overcome the mesh dependency issue which may exist in other local damage models. Accordingly, the crack initiation, crack propagation, and most importantly, the interaction among multiple cracks can be captured conveniently. The crack trajectory is not necessarily be tracked by using the phase field model, and this has brought great advantages over some of the other widely adopted methods for modelling crack propagation such as the XFEM and cohesive element method [18, 23]. At the meso-scale, phase field model has been applied successfully to fiber-reinforced composites [24] and other heterogeneous materials [25, 26] under the uniaxial tensile and bending loads. Zhang et al. [27] applied the phase field model to multi-phase materials by which both matrix cracking and interfacial debonding can be captured. Zhang et al. [28] further demonstrated that, the explicit phase field model developed in the framework of dynamic mechanics could greatly improve the modelling capability for large sized models with up to 60 million DOFs. To date, the phase field method has not been employed to address the corrosion-induced concrete cracking problem. A meso-scale phase field model with the capacity of simulating arbitrary cracking and crack interactions in concrete will provide new insights into the degradation and failure of RC structures subjected to corrosion of multiple reinforcements.

This paper establishes a new numerical method to investigate the whole structural cover cracking induced by corrosion of multiple reinforcements, considering concrete as a heterogeneous material. A phase field model for concrete cracking at the meso-scale is first developed and interface regularization is made to address the discontinuity of interfacial properties. A special degradation function is used to consider the rapid change of fracture toughness over the ITZ. The numerical method is implemented into ABAQUS explicit regime through an in-house VUEL subroutine. A non-uniform corrosion model is employed to formulate the rust expansion around the steel reinforcing bars. An example for RC beam with three tensile reinforcements is presented to demonstrate the application of developed method. Repeatability of results and effects of aggregate randomness are also discussed. The model is then verified by comparing the results with those from experiments. Moreover, a parametric study is carried out to investigate the effects of reinforcement spacing, cover thickness, ITZ fracture properties on the crack pattern and the development of crack width over service time. Finally, the computational expense and possible ways to reduce the computational expense are discussed.

2. Meso-scale Phase Field Model for Concrete Cracking

2.1 Dynamic phase field model

Considering the domain Ω shown in Figure 1(a), Γ_i and Γ_c represent interface and crack domains, respectively. An external loading $\boldsymbol{t}^*$ is acting on the boundary $\partial\Omega_t$, whereas the boundary $\partial\Omega_u$ is subjected to a prescribed displacement. With the introduction of the phase field $d(\boldsymbol{x})$, the crack is regularized into a smeared damage zone, according to the theory of phase field model. The system's Marigo-Francfort potential functional is specified as follows:

$$W = \int_{\Omega_{mix}} \omega(d)\psi_\varepsilon \mathrm{d}V + \int_{\Omega_{mix}} G_s\gamma(d,\nabla d)\mathrm{d}V + \int_{\Omega_{inc}} \psi_\varepsilon \mathrm{d}V - W_{ext} \quad (1)$$

In the above equation, ψ_ε is the elastic potential density and the first term is the elastic potential, the second term is the fracture energy, the third term is the aggregate's elastic potential, and the fourth term is the external work potential. $\omega(d)$ is the degradation function which is used to account for the elastic property reduction due the damage. The function $\gamma(d,\nabla d)$ is the surface density function used to calculate the dissipated fracture energy for creating new crack surfaces. G_s is the critical energy release rate (CERR), also known as fracture energy. It is assumed that cracks evolve only in the mortar and the interface, so the aggregate is always intact and the degradation function is not applied to it. In this study, we choose to use a cohesive phase field model proposed by Wu [29], and the explicit forms of $\omega(d)$ and $\gamma(d,\nabla d)$ are available in [29]. According to the existing study [22] and the loading condition, it is necessary to split the potential energy into two parts, i.e., the tensile part ψ_ε^+ and the compressive part ψ_ε^-, while only the tensile part contributes to the evolution of damage. In addition, a historic variable H is introduced to prevent the physically unreasonable self-healing phenomenon. With the modifications mentioned above, the first term of Equation (1) can be changed as follows:

$$W = \int_{\Omega_{mix}} \omega(d) H + \psi_\varepsilon^- \mathrm{d}V \,, \; H = \max_{\tau \in [0,t]} \left\{ \psi_b^+ \left(\boldsymbol{\varepsilon}\left(\boldsymbol{x}, \tau \right) \right) \right\} \tag{2}$$

In the framework of dynamics, the system's Lagrange functional consists of potential energy and kinematic energy, specified as follows:

$$\begin{aligned} L\left(\boldsymbol{u}, \dot{\boldsymbol{u}}, d, \dot{d}\right) = \frac{1}{2}\int_\Omega \rho \dot{\boldsymbol{u}} \dot{\boldsymbol{u}} \mathrm{d}V + \int_T \int_\Omega \frac{1}{2} \bar{\eta} \dot{d}^2 \mathrm{d}V \mathrm{d}t - \int_{\Omega_{mix}} \omega(d) H + \psi_\varepsilon^- \mathrm{d}V \\ - \int_{\Omega_{mix}} G_s \gamma\left(d, \nabla d\right) \mathrm{d}V - \int_{\Gamma_c} G_s \mathrm{d}S - \int_{\Omega_{inc}} \psi_\varepsilon \mathrm{d}V + W_{ext} \end{aligned} \tag{3}$$

where the first term is the kinematic energy and the second term is the viscosity phase field energy originally introduced in [22]. $\bar{\eta}$ is an artificial viscosity parameter and T is the total time. Let $\boldsymbol{q} = [\boldsymbol{u}, d]$ and $\dot{\boldsymbol{q}} = [\dot{\boldsymbol{u}}, \dot{d}]$, the system's Lagrange equation can be derived through the following equation:

$$\frac{\mathrm{d}}{\mathrm{d}t}\left(\frac{\partial L}{\partial \dot{\boldsymbol{q}}} \right) - \frac{\partial L}{\partial \boldsymbol{q}} = 0 \tag{4}$$

The numerical solution of the coupled phase field equation is normally solved with the finite element method, the displacement and phase fields inside an element can be expressed with the nodal values through proper interpolation. The finite element method governing equation of the dynamic phase field model is specified as follows:

$$\boldsymbol{M} \ddot{u}^N = \boldsymbol{P}_{ext} - \boldsymbol{P}_{int} \,, \; \boldsymbol{C} \dot{\boldsymbol{d}}^N = \boldsymbol{Y}\left(\boldsymbol{u}, d \right) \tag{5}$$

Explicit forms of the matrices are referred to [28]. The equation of displacement is solved by using central difference method while the phase field equation is solved with the forward difference method. With the aid of the lumped mass matrix $\boldsymbol{M}$ and the lumped viscosity matrix $\boldsymbol{C}$, Equation (5) can be solved with the explicit time integration scheme which has tremendously high efficiency in comparison with the widely used implicit schemes. More details about the phase field model can be found in our previous studies on modelling fiber-reinforced composites [24, 28].

2.2 Meso-scale concrete and interface regularization

At the meso-scale, concrete is a typical heterogeneous material that consists of aggregates, cement mortar and the ITZ. Such a heterogeneous structure of concrete with variation in mechanical properties can induce some toughening mechanisms during the concrete crack propagation process, e.g., aggregate bridging, micro-cracks shielding, crack deflection, etc. [30-32]. Therefore, we establish a three-phase model consisting of aggregates, mortar and ITZ to simulate the meso-scale concrete cracking. The aggregates are simplified as polygons with a random size and 4 to 13 sides. For simplicity, only coarse aggregates larger than 2.4 mm are modelled, while fine aggregates and cement are treated as the mortar phase [17]. The total fraction of coarse aggregates accounts for about 40% of the whole volume of concrete. A typical three-segment gradation size distribution [33] in Table 1 is employed to control the aggregates size distribution. Further, the two-dimensional distribution of aggregates can be calculated according to the Walraven formula [34, 35]:

$$\mathrm{P}(D < D_0) = \mathrm{P}_k(1.065\left(\frac{D_0}{D_{max}}\right)^{0.5} - 0.053\left(\frac{D_0}{D_{max}}\right)^{4} - 0.012\left(\frac{D_0}{D_{max}}\right)^{6} - 0.0045\left(\frac{D_0}{D_{max}}\right)^{8} + 0.0025\left(\frac{D_0}{D_{max}}\right)^{10}) \quad (6)$$

where $\mathrm{P}(D < D_0)$ is the probability of the aggregate diameter D in a cross-sectional plane smaller than D_0; D_{max} is the maximum diameter of aggregates. The calculated 2D distribution of coarse aggregates is also listed in Table 1.

The change of material properties on the interface (Figure 1a) has brought considerable challenges in the numerical modelling. The thickness of ITZs between aggregates and mortar is normally only tens of microns. Modelling such a small thickness of ITZs will result in very dense meshes or distortions of adjacent elements for mortar and aggregates. There are two common approaches to model ITZs: (1) using zero-thickness interface elements for ITZs [17, 18]; (2) setting the thickness of ITZs 0.1-1 mm [36-37]. In this study, we set the ITZ thickness as 0.5 mm. Further, an interface regularization scheme reported in [24, 27] is employed to model the mechanical properties of ITZs. The scheme introduces an auxiliary phase field $\eta(x)$ to convert the interface into a smeared strip with certain width, as shown in Figure 1(b). The equivalent material properties are considered smoothly distributed in the smeared zone and are composed of that of the interface and matrix. More details on deriving $\eta(x)$ are referred to [24, 27]. The equivalent strength $\sigma_{\max}^{s}$ is specified as follows:

$$\sigma_{\max}^{s}(\eta) = \sigma_{\max}^{i}\left[1 - h(\eta)\right] + \sigma_{\max}^{m} h(\eta) \tag{7}$$

whereas the equivalent critical energy release rate (CERR) or fracture energy is given as follows:

$$G_s(\eta) = \left[1 - h(\eta)\right] \int_0^D \left\{G_i\left[1 - h(\eta)\right] + G_m h(\eta)\right\} \frac{1}{c_0}\left(\frac{\alpha(d)}{l_0} + l_0 |\nabla d|^2\right) \mathrm{d}x + G_m h(\eta) \tag{8}$$

where $D = \pi l_0 / 2$. The subscripts "*i*" and "*m*" represent interface and matrix, respectively and "*s*" represent the equivalent property in the smeared zone. $h(\eta)$ should be chosen to ensure a monotonic change of the material properties. In the previous study, a quadratic form of degradation function was used, as follows

$$h(\eta) = (1 - \eta)^2 \tag{9}$$

With this degradation function, the fracture energy in Equation (8) changes smoothly but slowly. As a result, any change of the fracture energy with small quantity (especially for the interface) may not have a significant impact on the fracture energy, and thus cannot be reflected in the modelling result. In this study, we propose to use an exponential form of degradation function, as given by

$$h(\eta)=\frac{1-e^{-k(1-\eta)^n}}{1-e^{-k}},\ k>0,\ n\geq 2 \tag{10}$$

With the new degradation function, the equivalent CERR is enhanced. As an example, we assume equivalent CERRs of interface and matrix are 0.02 N/mm and 0.07 N/mm, respectively. The obtained equivalent CERR is shown in Figure 2. The new degradation function maintains a short region in which the equivalent CERR is almost equal to the interface, and the value then has a rapid but smooth transition to that of the matrix. In this way, the change of material property can be reflected in the modelling result and the mesh density near the ITZ zone can be relaxed. The length of the front region and the slope of the equivalent CERR shown in Figure 2 can be adjusted by the two parameters, k , n , and in this study we choose $k=5000000,\ n=140$.

2.3 Numerical implementation

The theory is implemented into ABAQUS EXPLICIT through the users' subroutine VUEL, and MPI parallel calculation available in ABAQUS. MPI parallel calculation is normally known inapplicable when a user defined element is used is enabled and in our simulation this is achieved through programing the VUEL codes with the special consideration of parallel calculation. One issue when using the explicit integration scheme is the determination of stable time interval Δt_c. Smaller time intervals can bring additional computational costs but higher ones could result in unexpected wrong predictions. For central difference method, the critical stable time interval is

$$\Delta t_u \approx \frac{L_{\min}}{c_d},\ c_d = \sqrt{\frac{\lambda + 2\mu}{\rho}} \tag{11}$$

where $L_{\min}$ is the minimum mesh size, c_d is the wave speed, and for isotropic material, ρ is mass density and λ and μ are Lame constants. For forward difference method, the critical time interval is specified by:

$$\Delta t_d \approx \frac{L_{\min}^2}{2\alpha} \tag{12}$$

where $\alpha = 2l_0 G_s / c_0 \bar{\eta}$, $c_0 = 4\int_0^1 \sqrt{\alpha(s)}ds$. For the coupled displacement-phase field problem, the adopted time interval is

$$\Delta t_c \approx \kappa \cdot \min\left\{\Delta t_u, \Delta t_d\right\} \tag{13}$$

where $\kappa \in (0,1]$ is a safety parameter and we use $\kappa = 0.5$ in this study.

3. Non-uniform Corrosion Model and Crack Width Calculation

3.1 Non-uniform corrosion model

The reinforcing bar in concrete is normally in passive state due to the alkali environment in concrete. In the chloride-laden environment, the depassivation and corrosion of reinforcing bar can occur once the chloride content near the reinforcement reaches a critical value. Due to the differences in the diffusion routes from different sides of RC structures, the part of steel bar near the concrete cover surface will firstly be corroded and has a higher corrosion rate. Evidently, the corrosion rust development of reinforcing bar in concrete is non-uniform. Considerable experiments and electrochemical corrosion simulations have proved that, more corrosion products accumulate around the half of reinforcing bar near the cover surface while almost no corrosion product can be observed at the other part [38-43]. Therefore, we formulate one of the most widely accepted non-uniform corrosion model, i.e., the semi-elliptical corrosion model [40], to investigate corrosion-induced concrete cover cracking.

Previous studied [44, 45] have found that, there is a porous zone or corrosion accommodation zone with a thickness of 10-50 μm at the interface between the concrete and reinforcing bar. Corrosion products will first fill into the porous zone without the expansion force. Therefore, the porous zone is considered as a porous circular band in the model. Figure 3 illustrates the distribution of corrosion products around the reinforcing bar. The total amount of corrosion products are divided into three parts: (1) the semi-elliptical band of corroded steel with maximum thickness $d_{co\text{-}st}$; (2) the porous circular band d_0; (3) the semi-elliptical rust band with maximum thickness d_m. The front of the corrosion is in a semi-elliptical shape with the semi-major axis equal to $\phi/2+d_0+d_m$ and the semi-minor axis $\phi/2+d_0$. Considering the boundary of original reinforcing bar, the expansion displacement of rust driving concrete cracking can be expressed as follows:

$$r(\theta)=\frac{(\Phi+2d_0+2d_m)(\Phi+2d_0)}{\sqrt{(2\Phi+4d_0)^2+16d_m(\Phi+2d_0+d_m)(cos\theta)^2}}-\frac{\Phi}{2}-d_0 \tag{14}$$

where θ is the location angle of rust in the polar coordinates system ($0\le\theta\le\pi$). Φ is the diameter of the reinforcing bar. The rust expansion function $r(\theta)$ will be the displacement boundary condition in the following numerical models. More details on the semi-elliptical corrosion model can be found in [40, 46].

Further, the corrosion degree or steel loss ratio can be expressed as follows [11]:

$$\eta=\frac{(d_m+2d_0)\alpha_{rust}\rho_{rust}}{(\rho_{st}-\alpha_{rust}\rho_{rust})\Phi} \tag{15}$$

where ρ_{rust} and ρ_{st} are the densities of rust and steel, respectively; α_{rust} is the molecular weight of steel divided by the molecular weight of corrosion products.

3.2 Determination of crack width

Crack width is one of the most significant parameters for the design and assessment of RC structures. For instance, the crack width 0.3 mm is regarded as critical crack width for RC structures exposing in the humidity, moist air, soil conditions [47]. Therefore, a numerical algorithm to calculate the crack opening displacement is proposed to determine the crack width.

Considering a bar in the region $x \in [0, L]$, the left side is fully fixed, the right side is subjected to tensile loading with specific displacement u^*, as shown in Figure 4(a). Without consideration of body force, the real stress σ_r distributes uniformly along the bar, and the displacement u^* can be represented as follows:

$$u^* = \int_0^L \varepsilon dx \tag{16}$$

where $\varepsilon = \dfrac{\sigma_n}{E_0}$ is the total strain, σ_n is the nominal stress, E_0 is the initial elastic modulus. The total strain is assumed to be composed of two parts, i.e., elastic strain and damaged strain. Accordingly, Equation (16) can be rewritten as follows:

$$u^* = \int_0^L \frac{\sigma_r}{E_0} \mathrm{d}x + \int_0^L \frac{\sigma_n - \sigma_r}{E_0} \mathrm{d}x \tag{17}$$

According to the phase field model, the real stress can be calculated through $\sigma_r = \omega(d)\sigma_n$; thus Equation (16) can be changed as follows:

$$u^* = \int_0^L \frac{\sigma_r}{E_0} \mathrm{d}x + \int_0^L \frac{\sigma_n}{E_0} (1 - \omega(d)) \mathrm{d}x = \frac{\sigma_r}{E_0} L + \int_0^L \varepsilon (1 - \omega(d)) \mathrm{d}x \tag{18}$$

Obviously, the second term is the crack opening displacement,

$$w = \int_0^L \varepsilon (1 - \omega(d)) \mathrm{d}x \tag{19}$$

We can extend this theory to 2D and 3D cases for calculating the crack opening displacement.

Taking a 2D case shown in Figure 4(b) as an example and after obtaining the phase field distribution, the crack opening displacement along the horizontal direction can be given as follows:

$$w = \sum_{i=1}^{4} \left[u(i+1) - u(i) \right] \left[1 - \frac{\omega(i+1) + \omega(i)}{2} \right] \tag{20}$$

4. Worked Example and Verification

To demonstrate the numerical method, a two-dimensional reinforced concrete beam model with three tensile reinforcing bars is developed. Figure 5 shows the RC beam model with dimensions of 400 mm in height and 196 mm in width. The diameter of reinforcement is 12 mm. The cover thickness is 20 mm and the clearing space of reinforcements is 60 mm. To reduce the computational time, only the top area with the potential of cracking is established as the heterogeneous model while the other part is taken as homogenous and elastic. All the basic mechanical and corrosion parameters are given in Table 2. The semi-elliptical non-uniform corrosion model, i.e., Equation (14), is worked as a displacement boundary condition in the numerical model. Based on the assumption that chlorides, as well as other essential ions, such as oxygen and moisture, penetrated through the concrete cover from one side only, e.g. the splashing wave side, the corroded half of steel bar is facing the top surface of the beam (shown in Figure 5).

Figure 6 shows the cracking process of concrete caused by the non-uniform corrosion of reinforcements. To clearly show the micro and macro cracks in the model, the elements with a phase field value larger than 0.9 are marked as red. It can be seen that, when the corrosion degree increases to 0.37%, some micro cracks appear in the interfaces between the aggregates and mortar. Moreover, surface cracks are first initiated at the top of the two corner reinforcements. With the development of corrosion, cracks around the middle reinforcement propagate towards the corner reinforcements and cracks around the corner reinforcements propagate towards the middle-located reinforcement (Figure 6b). When the corrosion degree is increased to 0.73% (i.e., Figure 6c), two side cracks appear in the left and right cover of concrete and propagate outwards, which will make a corner spalling failure. Finally, the side cracks will be connected to form a through crack and the delamination of cover will occur (Figure 6d).

Figure 7 illustrates the energy evolution during the development of corrosion process. The external energy is the total work done by the expansion of corrosion products. The elastic energy is the recoverable deformation energy of concrete. The fracture energy is the energy consumed by concrete cracking. The kinetic energy is associated with dynamic motion. To accurately model a quasi-static problem by ABAQUS/Explicit, the kinetic energy should a small fraction (typically 5–10%) of external energy. It can be seen that, the kinetic energy during the whole simulation is close to zero, which ensures the loading is a quasi-static process in the simulation. The corrosion products expansion transfers to external energy of the beam, of which the elastic deformation energy and fracture energy account most. At the initial corrosion stages (0-0.3%), the fracture energy is close to the elastic energy when lots of micro cracks of concrete appear. After that, the ratio of elastic energy to fracture energy becomes larger when the macro cracks have formed and the crack width is increasing.

To investigate the effect of aggregate randomness on the numerical results, 10 meso-scale models with the same grading and aggregates fraction are established to simulate corrosion-induced concrete cracking. Figure 8 shows the typical crack patterns of the RC beam caused by the non-uniform corrosion. It can be seen that, the overall failure patterns are very similar, i.e., delamination and corner spalling of concrete cover. As expected, the aggregates in concrete affects the location of micro and macro cracks because the weak interfaces between aggregates and mortar dominates the crack initiation and connections. Moreover, the developed model well reproduces the crack deflection, aggregate/mortar bridging and crack bifurcation phenomena during concrete cracking (e.g., Figure 8). Crack deflection occurs when a potential crack path of least resistance is around an aggregate or a weak interface. Aggregate bridging occurs when two or more cracks propagate along two sides of aggregates and advance beyond the aggregates. Mortar bridging appears when two cracks propagate along the sides of neighboring aggregates. Crack bifurcation appears when a crack deflects into different sides of an aggregate or different aggregates. It can be concluded that, the ITZs in concrete dominate the fracture propagation of concrete at the meso-scale. The developed meso-scale model is advantageous compared with most existing concrete fracture models [16, 39, 48], in terms of capturing toughening mechanisms and arbitrary cracking paths. Figure 9 illustrates the surface crack width developments at the top of two corner reinforcements for the 10 random models. It can be seen that, the surface crack width begins to increase when the corrosion degree reaches to about 0.08%. Then the crack width gradually increases with the development of corrosion. When the corrosion degree is about 0.62-0.75%, the surface crack width reaches 0.3 mm. The numerical results have a good repeatability for different random models.

To verify the developed numerical method on the crack width development, experimental results from Ye et al. [38] are used for comparison. In the experiment, the rust distribution of C20 specimens was non-uniform and the crack width development as a function of corrosion degree was given. The geometric and mechanical parameters are listed in Table 3. Figure 10 shows the crack width developments from numerical and experimental results. It can be seen that, the numerical results have a good agreement with the experimental results. It should be mentioned that, the crack width from experiments are obtained by using a binocular lens with a measuring precision of 0.01 mm [38]. Therefore, the error when measuring a very small crack width could result in the differences between experimental and numerical results at the initial stage (crack width smaller than 0.02 mm).

To verify the developed numerical method on the crack patterns induced by multiple reinforcement corrosion, experimental results from Zahid et al. [49] are used for comparison. In their experiments [49], concrete panels of dimensions 600 × 600 × 150 mm with five reinforcements of 19 mm in diameter were made for corrosion tests. The cover thickness of Panels 1 and 2 are 30 mm. Electrochemical accelerated corrosion was applied to five reinforcements in Panel 1 for 45 days and middle three reinforcements in Panel 2 for 56 days. The volume proportion of coarse aggregates for the concrete specimens are about 40%. The compressive strength and elastic modulus of the concrete specimens are 42 MPa and 35 GPa, respectively. The geometric and mechanical parameters in the numerical model are listed in Table 4. Consistent with the experiment set-up, corrosion expansions for all five reinforcements are modelled for Panel 1 while only the middle three reinforcements corrosion is modelled for Panel 2. Figure 11 shows the crack patterns from experimental and numerical results. It can be seen that the numerical results have a good agreement with experimental results. For Panel 1 with five reinforcement corrosion, a through crack is formed and connected to make concrete delamination. Only two vertical surface cracks from at the top of two side reinforcements. This is because the through crack releases stress concentration and stops concrete surface cracking at the top of middle reinforcements. For Panel 2 with only middle three reinforcement corrosion, two vertical cracks form at the top of corroded side reinforcements. Experimental and numerical results both show that, surface cracking is more prone to form for corroded corner reinforcement.

5. Parametric Study and Discussion

The clearing space of reinforcement is an important parameter for the design of RC structures. Figure 12 shows the crack patterns of concrete for the clearing spaces of reinforcements, 30 mm, 60 mm and 90 mm, respectively. It can be seen that, delamination failure of concrete cover occurs for the three cases but the smaller the clearing space of reinforcements is, the more complex the crack network is. For the clearing space 30 mm, the aggregate bridging and parallel cracks occur at the middle of concrete cover. While for the relatively large clearing space of reinforcements (i.e., 60 and 90 mm), the side cracks are more prone to connect to form a through crack. Figure 13 illustrates the surface crack width development for different clearing space of reinforcements. It can be found that, the larger the clearing space is, the larger the surface crack width is. A significantly drop of the surface crack width occurs when the through crack is formed for the clearing space 90 mm. Therefore, the through crack will affect concrete surface crack development. Figure 14 shows the effect of the clearing space on the ratios of fracture energy to external energy and elastic energy to external energy. Generally, the larger the clearing space is, the larger the energy ratio is. Therefore, more external energy caused by corrosion is transferred to elastic energy for the RC structures with a smaller reinforcement clearing space. Therefore, it is helpful for reducing the clearing space of reinforcements to maximize the using of materials and prolong the service life of RC structures under corrosive environments.

Figure 15 shows the crack patterns of concrete for cover thicknesses 20 mm, 30 mm and 40 mm. It can be seen that, the crack patterns of concrete are all delamination and corner spalling, i.e., a horizontal through crack make the middle part of concrete delaminate, and top and side cracks around the corner rebar make corner spalling. For non-uniform corrosion of reinforcements, more corrosion products accumulate around the half of reinforcement facing concrete cover, which produces concentrated tensile stress to make cover delaminate. Figure 16 illustrates the crack width developments for different cover thicknesses. It can be found that, the smaller the cover thickness is, the smaller the corrosion degree to surface cracking is. The initial surface crack width (<0.1 mm) is larger for a smaller cover thickness. With the crack width increasing, the difference of crack width for different cover thicknesses becomes negligible.

It is very challenging to measure the fracture properties of ITZ, especially fracture energy, through experiments [50-52]. Moreover, the tensile strength and fracture energy of ITZ are dependent on the aggregate type, roughness and curing conditions [52-54]. Therefore, it is worthy to investigate the effect of ITZ fracture properties on corrosion-induced concrete cracking. Figure 17 shows the crack patterns of concrete for tensile strengths of ITZ 0.1 MPa, 0.25 MPa and 1 MPa which are about 1/20-1/2 of mortar tensile strength with reference to [52-52]. The other parameters including fracture energy of ITZ keep the same as those in the worked example (see Table 2). It can be seen that, two failure modes (i.e., delamination and corner spalling) occurs for the concrete beam with different ITZ strengths. With a lower ITZ strength, the top crack is less likely to form and the concrete cover is more prone to be delaminated by corrosion-induced horizontal through cracks. Therefore, the ITZ strength significantly affects the failure mode of corrosion-induced concrete beam cracking, which also proves the necessity and value of modelling corrosion-induced concrete beam cracking at the meso-scale. Figure 18 illustrates the crack width development for different ITZ strengths. It can be seen that, for low ITZ strengths, the top surface crack firstly increases to about 0.03 mm then gradually decreases to about zero. The lower the ITZ strength is, the faster the top surface crack closes. This is because the side crack releases stress concentration on the top of concrete cover and the side crack propagates faster for a lower ITZ strength. Figure 19 shows the crack patterns of concrete cover for different fracture energies of ITZ. The ITZ fracture energies are chosen as 0.00525 N/mm, 0.0105 N/mm and 0.021 N/mm which are about 0.07-0.3 time of mortar fracture energy after previous experimental results [52]. The other parameters including tensile strength of ITZ keep the same as those in the worked example (see Table 2). It can be seen that, horizontal through cracks form in the concrete cover for the three values of ITZ fracture energy, which makes the middle of concrete covers delaminate. However, for the smallest fracture energy (see Figure 19a), the left upper surface crack does not appear. Figure 20 illustrates the crack width developments for different fracture energies of ITZ. It can be seen that, for ITZ fracture energy 0.00525 N/mm, the crack width at the left top surface of the beam firstly increases to 0.02 mm but gradually decreases to about zero. For other cases, the ITZ fracture energy has little effect on the crack width development. Therefore, fracture energy of ITZ can also change the corrosion–induced cracking pattern. The stronger the ITZ is (i.e., larger strength and fracture energy), the corner spalling of concrete cover is more likely to occur for RC beam with multiple reinforcements.

6. Computational expense

Considering that the corrosion induced concrete fracture is a quasi-static process and the present explicit phase field model is developed under the framework of dynamic mechanics, the loading speed should be kept as small as possible to eliminate the dynamic effect. The computational expense, DOFs and results for the worked example are provided in Figure 21. There are 2,495,106 triangle elements for mortar and ITZs, 953,863 triangle elements for aggregates and 737,696 triangle elements for homogeneous concrete in the model. Each node for mortar and ITZs elements has three displacement DOFs and one phase field DOF. The node for elastic aggregate and homogeneous concrete only has three displacement DOFs. The total DOF in the worked example is 40,090,626. The mesh size for the interested meso-scale part is

0.1 mm. Here we compare three different ways utilizing less consumed time, i.e., (1) using less loading time to model the same physical process (the standard loading time is 0.05s which is used as the reference and we use 0.01s in this case. Time is fictitious here; (2) using less loading time and using artificial damping to the system and; (3) using a digital filter (low pass Butterworth filter) to remove high frequency components from the results in (1). The definition of the damping is specified by

$$\left(\sigma_{vis}\right)_j = \begin{cases} b_1 \rho c_d L_e \dot{\varepsilon}_j - \rho \left[b_2 L_e \left\langle \dot{\varepsilon}_j \right\rangle_- \right]^2, & \text{for } j = 1,2 \\ 0, & \text{otherwise} \end{cases} \tag{21}$$

where $\dot{\varepsilon}_j = \partial \varepsilon_j / \partial t$, c_d is the wave speed, L_e is the characteristic length of the element, and b_1 and b_2 are viscosity parameters, here we use $b_1=0.12$ and $b_2=2.4$.

From the result in Figure 21 (a) and (b), all the three approaches have reduced the consumed time since the total load time step is reduced. Approach (1) has brought significant dynamic responses, as demonstrated by the waves in the curve. Approach (2) is closer to the result with more loading time. Approach (3) is closer to approach (1) and the curve is flatter. The dynamic response might contain contributions from both low and high frequencies, and the viscosity added to the system has attenuated the dynamic response. However, the filter only removed the high frequency's contribution. The filter could be used in case that the mechanics response is well understood and the parameters are well calibrated, as illustrated by the right half of the curve from approach (3) which is close to the reference.

7. Conclusions

In this paper, a meso-scale phase field model for concrete cover cracking under simultaneous corrosion of multiple reinforcements has been developed. A three phase (i.e., aggregates, mortar and interfaces) heterogeneous concrete model was considered and a regularization method was proposed to address interface properties when incorporated into the phase field model. The numerical model was implemented into ABAQUS EXPLICIT through an in-house VUEL subroutine. A non-uniform corrosion model based on previous experimental results was employed and a numerical algorithm was proposed to calculate the crack width. A concrete beam with three tensile reinforcements was presented to demonstrate the developed numerical method which was also verified through comparison with experimental results from the literature. It has been found that the developed model can well simulate arbitrary cracking and complex crack interactions. Some toughening mechanisms including crack deflection, aggregate/mortar bridging and crack bifurcation in concrete were captured. Further, parametric studies were carried out to investigate effects of reinforcement spacing, cover thickness and ITZ properties on concrete cover cracking. The larger the reinforcement spacing is, the horizontal through crack is more prone to connect and more external energy caused by corrosion is transferred to fracture energy. The fracture properties of ITZ significantly affects the cracking patterns of concrete cover. The stronger the ITZ is (i.e., larger strength and fracture energy), the corner spalling of concrete cover is more likely to occur. The numerical model presented in the paper can be used to simulate the meso-scale fracture of RC structures subjected to non-uniform corrosion of multiple reinforcements.

ACKNOWLEDGEMENTS

Partial financial support from the UK Engineering and Physical Sciences Research Council (EP/S005560/1) is gratefully acknowledged. The Visiting Professorship from Dalian University of Technology to ST Yang is also thankfully acknowledged.

REFERENCES

[1] U.M. Angst, Challenges and opportunities in corrosion of steel in concrete, Mater. Struct. 51(4) (2018) 1-20.

[2] Z.P. Bazant, Physical model for steel corrosion in concrete sea structures - theory, Journal of the Structural Division-ASCE 105(6) (1979) 1137-1153.
[3] C. Andrade, F.J. Molina, C. Alonso, Cover cracking as a function of rebar corrosion: Part 1-experiment test, Mater. Struct. 26 (1993) 453-454.
[4] K. Vu, M.G. Stewart, J. Mullard, Corrosion-induced cracking: Experimental data and predictive models, ACI Structural Journal 102(5) (2005) 719-726.
[5] C.Q. Li, R.E. Melchers, J.J. Zheng, Analytical model for corrosion-induced crack width in reinforced concrete structures, ACI Structural Journal 103(4) (2006) 479-487.
[6] C.Q. Li, S.T. Yang, Prediction of concrete crack width under combined reinforcement corrosion and applied load, J. Eng. Mech. 137(11) (2011) 722-731.
[7] C. Lu, W. Jin, R. Liu, Reinforcement corrosion-induced cover cracking and its time prediction for reinforced concrete structures, Corros. Sci. 53(4) (2011) 1337-1347.
[8] J. Chen, W. Zhang, X. Gu, Modeling time-dependent circumferential non-uniform corrosion of steel bars in concrete considering corrosion-induced cracking effects, Eng. Struct. 201 (2019) 109766.
[9] X. Zhang, M. Li, L. Tang, S.A. Memon, G. Ma, F. Xing, H. Sun, Corrosion induced stress field and cracking time of reinforced concrete with initial defects: Analytical modeling and experimental investigation, Corros. Sci. 120 (2017) 158-170.
[10] K. Bhargava, A.K. Ghosh, Y. Mori, S. Ramanujam, Model for cover cracking due to rebar corrosion in RC structures, Eng. Struct. 28(8) (2006) 1093-1109.
[11] X. Xi, S. Yang, C.Q. Li, Accurate cover crack modelling of reinforced concrete structures subjected to non-uniform corrosion, Struct. Infrastruct. Eng. 14(12) (2018) 1628-1640.
[12] J. Zhang, X. Ling, Z. Guan, Finite element modeling of concrete cover crack propagation due to non-uniform corrosion of reinforcement, Constr. Build. Mater. 132 (2017) 487-499.
[13] Z. Cui, A. Alipour, Concrete cover cracking and service life prediction of reinforced concrete structures in corrosive environments, Constr. Build. Mater. 159 (2018) 652-671.
[14] X. Cheng, Q. Su, F. Ma, X. Liu, X. Liang, Investigation on crack propagation of concrete cover induced by non-uniform corrosion of multiple rebars, Eng. Fract. Mech. 201 (2018) 366-384.
[15] A. Chen, Z. Pan, R. Ma, Mesoscopic simulation of steel rebar corrosion process in concrete and its damage to concrete cover, Struct. Infrastruct. Eng. 13(4) (2016) 478-493.
[16] X. Xi, S. Yang, Time to surface cracking and crack width of reinforced concrete structures under corrosion of multiple rebars, Constr. Build. Mater. 155 (2017) 114-125.
[17] X. Xi, S. Yang, C.Q. Li, M. Cai, X. Hu, Z.K. Shipton, Meso-scale mixed-mode fracture modelling of reinforced concrete structures subjected to non-uniform corrosion, Eng. Fract. Mech. 199 (2018) 114-130.
[18] X. Xi, S. Yang, C.Q. Li, A non-uniform corrosion model and meso-scale fracture modelling of concrete, Cem. Concr. Res. 108 (2018) 87-102.
[19] P. Jiradilok, K. Nagai, K. Matsumoto, Meso-scale modeling of non-uniformly corroded reinforced concrete using 3D discrete analysis, Eng. Struct. 197 (2019).
[20] W. Ren, Z. Yang, R. Sharma, C. Zhang, P.J. Withers, Two-dimensional X-ray CT image based meso-scale fracture modelling of concrete, Eng. Fract. Mech. 133 (2015) 24-39.
[21] T.Q. Bui, X. Hu, A review of phase-field models, fundamentals and their applications to composite laminates, Eng. Fract. Mech. 248 (2021) 107705.
[22] C. Miehe, F. Welschinger, M. Hofacker, Thermodynamically consistent phase-field models of fracture: Variational principles and multi-field FE implementations, International Journal for Numerical Methods in Engineering 83(10) (2010) 1273-1311.
[23] Y. Huang, Y. Guan, L. Wang, J. Zhou, Z. Ge, Y. Hou, Characterization of mortar fracture based on three point bending test and XFEM, International Journal of Pavement Research and Technology 11(4) (2018) 339-344.

[24] P. Zhang, W. Yao, X. Hu, T.Q. Bui, 3D micromechanical progressive failure simulation for fiber-reinforced composites, Compos. Struct. 249 (2020) 112534.
[25] T.T. Nguyen, J. Yvonnet, Q.Z. Zhu, M. Bornert, C. Chateau, A phase-field method for computational modeling of interfacial damage interacting with crack propagation in realistic microstructures obtained by microtomography, Comput. Method. Appl. M. 312 (2016) 567-595.
[26] Z.J. Yang, B.B. Li, J.Y. Wu, X-ray computed tomography images based phase-field modeling of mesoscopic failure in concrete, Eng. Fract. Mech. 208 (2019) 151-170.
[27] P. Zhang, X. Hu, S. Yang, W. Yao, Modelling progressive failure in multi-phase materials using a phase field method, Eng. Fract. Mech. 209 (2019) 105-124.
[28] P. Zhang, W. Yao, X. Hu, X. Zhuang, Phase field modelling of progressive failure in composites combined with cohesive element with an explicit scheme, Compos. Struct. 262 (2021) 113353.
[29] J.Y. Wu, A unified phase-field theory for the mechanics of damage and quasi-brittle failure, Journal of the Mechanics and Physics of Solids 103 (2017) 72-99.
[30] J. Xiao, W. Li, D.J. Corr, S.P. Shah, Effects of interfacial transition zones on the stress–strain behavior of modeled recycled aggregate concrete, Cem. Concr. Res. 52 (2013) 82-99.
[31] W. Dong, Z. Wu, X. Zhou, L. Dong, G. Kastiukas, FPZ evolution of mixed mode fracture in concrete: Experimental and numerical, Eng. Failure Anal. 75 (2017) 54-70.
[32] S.P. Shah, S.E. Swartz, C. Ouyang, Fracture Mechanics of Concrete: Applications of Fracture Mechanics to Concrete, Rock, and Other Quasi-brittle Materials, John Wiley & Sons, Inc., New York, 1995.
[33] A.M. Neville, Properties of concrete, Fourth ed., Pearson Education Limited, London, 2006.
[34] J.C. Walraven, Aggregate Interlock: a theoretical and experimental analysis, Delft University Press, Delft, (1980).
[35] H. Ma, W. Xu, Y. Li, Random aggregate model for mesoscopic structures and mechanical analysis of fully-graded concrete, Comput. Struct. 177 (2016) 103-113.
[36] B. Šavija, M. Luković, J. Pacheco, E. Schlangen, Cracking of the concrete cover due to reinforcement corrosion: A two-dimensional lattice model study, Constr. Build. Mater. 44 (2013) 626-638.
[37] X. Du, L. Jin, R. Zhang, Modeling the cracking of cover concrete due to non-uniform corrosion of reinforcement, Corros. Sci. 89 (2014) 189-202.
[38] H. Ye, N. Jin, C. Fu, X. Jin, Rust distribution and corrosion-induced cracking patterns of corner-located rebar in concrete cover, Constr. Build. Mater. 156 (2017) 684-691.
[39] J. Chen, W. Zhang, Z. Tang, Q. Huang, Experimental and numerical investigation of chloride-induced reinforcement corrosion and mortar cover cracking, Cem. Concr. Compos. 111 (2020).
[40] Y. Yuan, Y. Ji, Modeling corroded section configuration of steel bar in concrete structure, Constr. Build. Mater. 23(6) (2009) 2461-2466.
[41] X. Xi, S. Yang, Investigating the spatial development of corrosion of corner-located steel bar in concrete by X-ray computed tomography, Constr. Build. Mater. 221 (2019) 177-189.
[42] D. Qiao, H. Nakamura, Y. Yamamoto, T. Miura, Crack patterns of concrete with a single rebar subjected to non-uniform and localized corrosion, Constr. Build. Mater. 116 (2016) 366-377.
[43] Y. Zhao, X. Zhang, H. Ding, W. Jin, Non-uniform distribution of a corrosion layer at a steel/concrete interface described by a Gaussian model, Corros. Sci. 112 (2016) 1-12.
[44] U.M. Angst, M.R. Geiker, A. Michel, C. Gehlen, H. Wong, O.B. Isgor, B. Elsener, C.M. Hansson, R. François, K. Hornbostel, R. Polder, M.C. Alonso, M. Sanchez, M.J. Correia, M. Criado, A. Sagüés, N. Buenfeld, The steel–concrete interface, Mater. Struct. 50(2) (2017).

[45] F. Chen, C.Q. Li, H. Baji, B. Ma, Quantification of steel-concrete interface in reinforced concrete using Backscattered Electron imaging technique, Constr. Build. Mater. 179 (2018) 420-429.
[46] S. Yang, X. Xi, K. Li, C.Q. Li, Numerical Modeling of Nonuniform Corrosion-Induced Concrete Crack Width, J. Struct. Eng. 144(8) (2018) 04018120.
[47] A.C.I. Committee, 224R-01: Control of Cracking in Concrete Structures (Reapproved 2008), Technical Documents.
[48] E. El Alami, F.E. Fekak, L. Garibaldi, A. Elkhalfi, A numerical study of pitting corrosion in reinforced concrete structures, Journal of Building Engineering 43 (2021).
[49] H.F. Zahid, P. Jiradilok, V. Singh Kuntal, K. Nagai, Investigation of the effects of multiple and multi-directional reinforcement on corrosion-induced concrete cracking pattern, Constr. Build. Mater. 283 (2021) 122594.
[50] L. Hong, X. Gu, F. Lin, Influence of aggregate surface roughness on mechanical properties of interface and concrete, Constr. Build. Mater. 65 (2014) 338-349.
[51] W. Dong, Z. Wu, X. Zhou, N. Wang, G. Kastiukas, An experimental study on crack propagation at rock-concrete interface using digital image correlation technique, Eng. Fract. Mech. 171 (2017) 50-63.
[52] G.A. Rao, B.K. Raghu Prasad, Influence of type of aggregate and surface roughness on the interface fracture properties, Mater. Struct. 37(5) (2004) 328-334.
[53] X. Gu, L. Hong, Z. Wang, F. Lin, Experimental study and application of mechanical properties for the interface between cobblestone aggregate and mortar in concrete, Constr. Build. Mater. 46 (2013) 156-166.
[54] X. Gu, J. Jia, Z. Wang, L. Hong, F. Lin, Determination of mechanical parameters for elements in meso-mechanical models of concrete, Frontiers of Structural and Civil Engineering 7(4) (2013) 391-401.
[55] W. Trawiński, J. Bobiński, J. Tejchman, Two-dimensional simulations of concrete fracture at aggregate level with cohesive elements based on X-ray μCT images, Eng. Fract. Mech. 168 (2016) 204-226.

LIST OF TABLES

Table 1 Three-segment gradation of aggregate size distribution [33-35]

Aggregate size (mm)	3D fraction in concrete	2D fraction in concrete
2.40-4.67	8.08%	6.2%
4.76-9.52	15.96%	8.7%
9.52-19.05	15.96%	9.8%

Table 2 Basic mechanical and corrosion parameters in the worked example [16, 17, 55]

Description	Values
Young's modulus of concrete	46 GPa
Poisson's ratio of concrete	0.22
Young's modulus of aggregate	80 GPa
Poisson's ratio of aggregate	0.16
Young's modulus of mortar	23 GPa
Poisson's ratio of mortar	0.22
Tensile strength of mortar	2.2 MPa
Fracture energy of mortar	0.072 N/mm
Young's modulus of ITZ	18 GPa
Poisson's ratio of ITZ	0.2
Tensile strength of ITZ	1 MPa
Fracture energy of ITZ	0.021 N/mm
Density of steel	7.85 mg/mm^3
Density of rust	3.6 mg/mm^3
Molecular weight ratio	0.57

689 Table 3 Values for variables used for comparison and validation of crack width development

690 [11, 38]

Description	Values
Top cover thickness	10 mm
Edge cover thickness	20 mm
Diameter of steel bars	10 mm
Poisson's ratio of aggregate	0.16
Length of specimen	100 mm
Height of specimen	100 mm
Young's modulus	18.82 MPa
Poisson's ratio	0.18
Tensile strength	5.725 MPa
Fracture energy	0.12 N/mm

Table 4 Values for variables used for comparison and validation of crack patterns [49]

Description	Values
Young's modulus of concrete	35 GPa
Poisson's ratio of concrete	0.2
Young's modulus of aggregate	70 GPa
Poisson's ratio of aggregate	0.2
Young's modulus of mortar	25 GPa
Poisson's ratio of mortar	0.2
Tensile strength of mortar	6 MPa
Fracture energy of mortar	60 N/m
Young's modulus of ITZ	12.5 GPa
Poisson's ratio of ITZ	0.2
Tensile strength of ITZ	3 MPa
Fracture energy of ITZ	30 N/m

LIST OF FIGURES

Figure 19 Crack patterns of concrete for different fracture energies of ITZ: (a) 0.00525 N/mm (b) 0.0105 N/mm; (c) 0.021 N/mm.

Figure 20 The crack width developments for different fracture energies of ITZ: (a) left top surface (b) right top surface.

Figure 21 Expensed time (a) and the modelling results (b) with different modelling approaches.

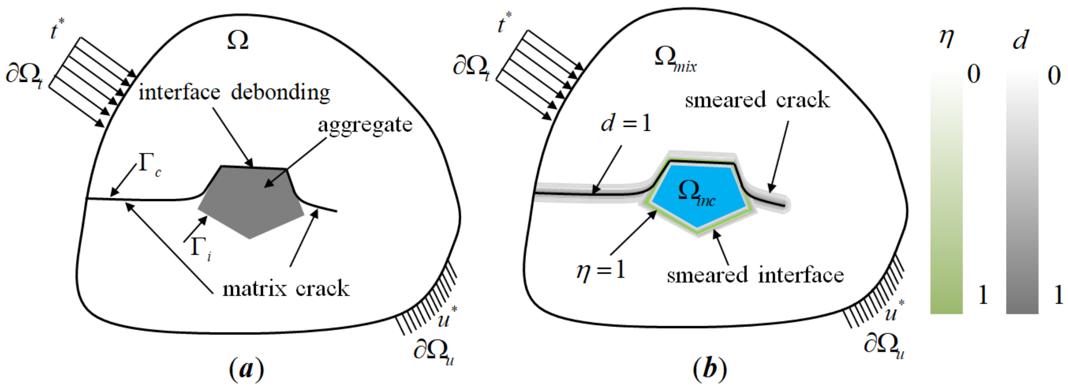

Figure 1 Representation of cracks and the interface (a) discrete model (b) smeared model.

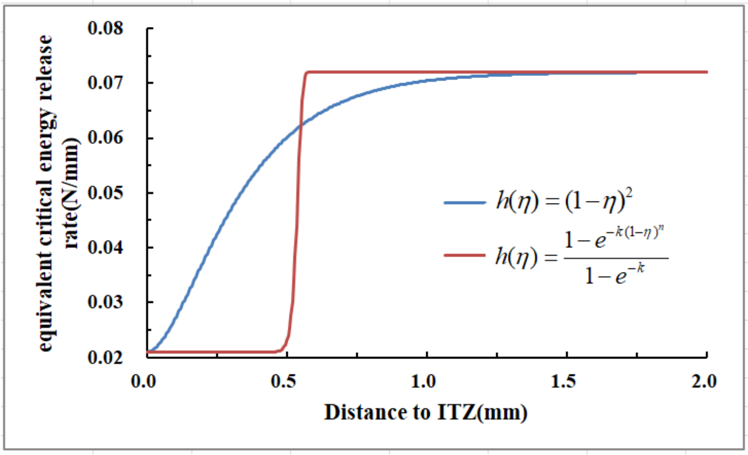

Figure 2 Equivalent Critical Energy Release Rate (k=5000000; n=140). The values of CERR for the interface and the matrix are 0.02 N/mm and 0.07 N/mm, respectively.

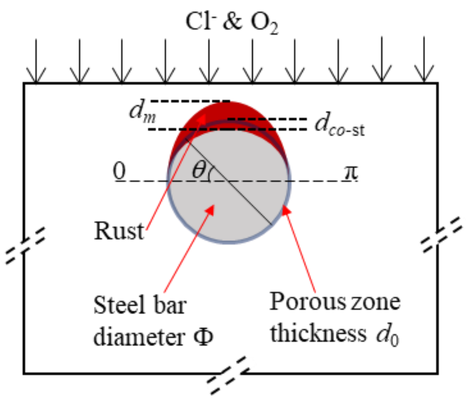

Figure 3 Semi-elliptical non-uniform corrosion model [40, 46].

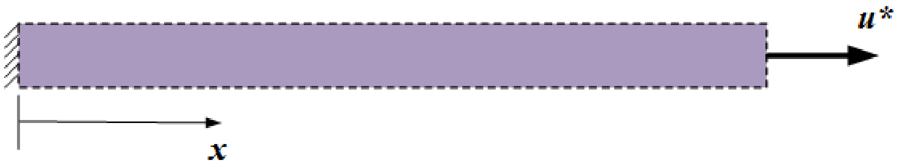

(a)

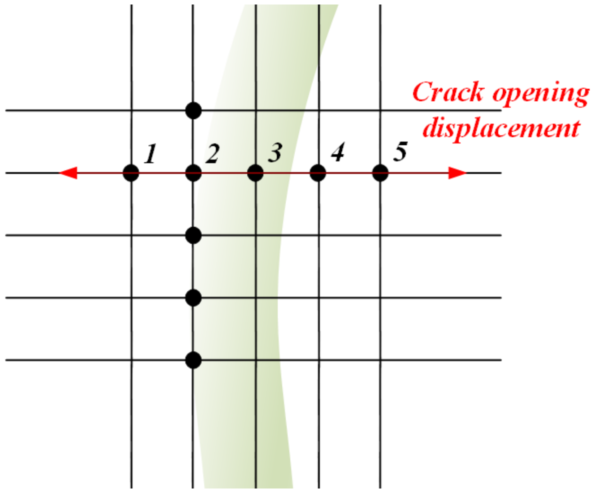

(b)

Figure 4 Determination of crack width: (a) A 1D bar to demonstrate the crack extension and (b) the way of estimation of the crack opening displacement in a 2D mesh.

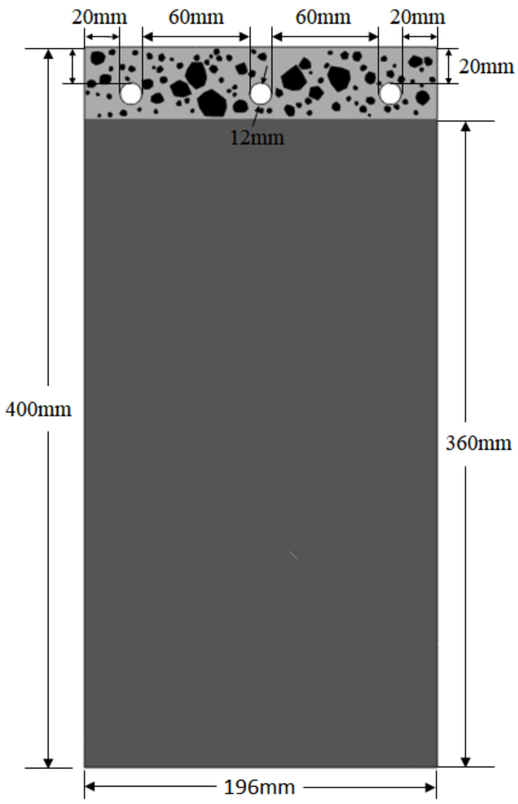

(a) Dimensions

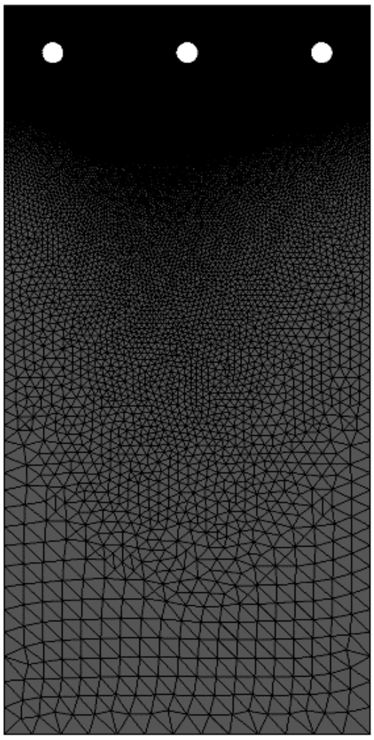

(b) Mesh

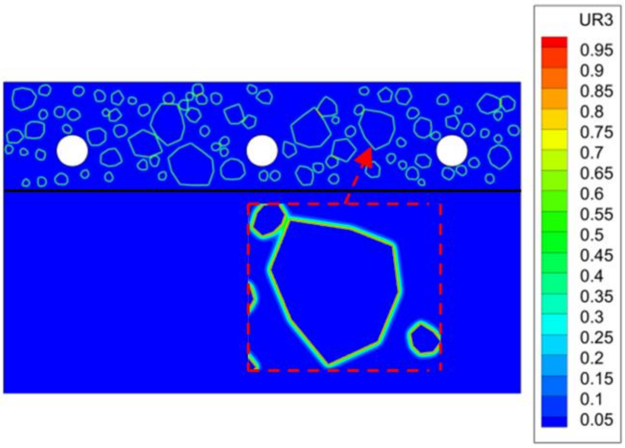

(c) Phase field's distribution

Figure 5 Worked example for RC beam with three reinforcements: (a) dimensions; (b) mesh; (c) the auxiliary phase field's distribution.

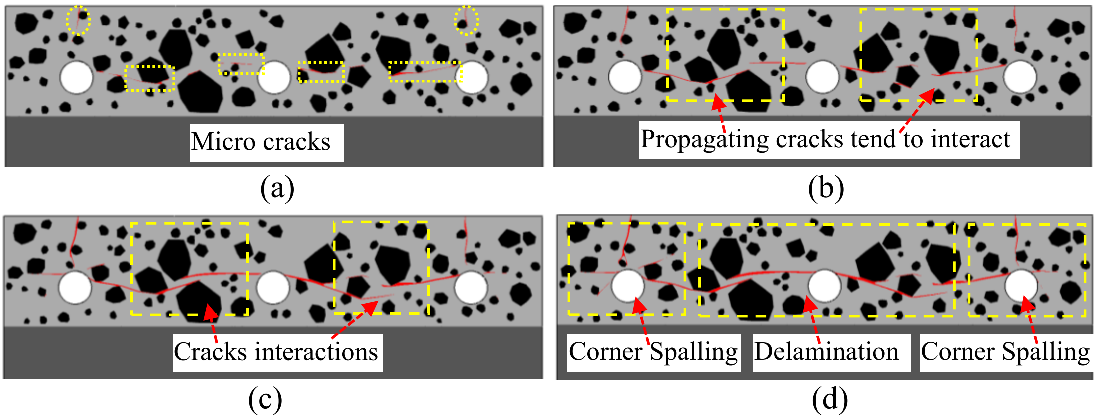

Figure 6 Crack development in concrete when corrosion degree reaches (a) 0.37%; (b) 0.51%; (c) 0.73%; (d) 0.81%.

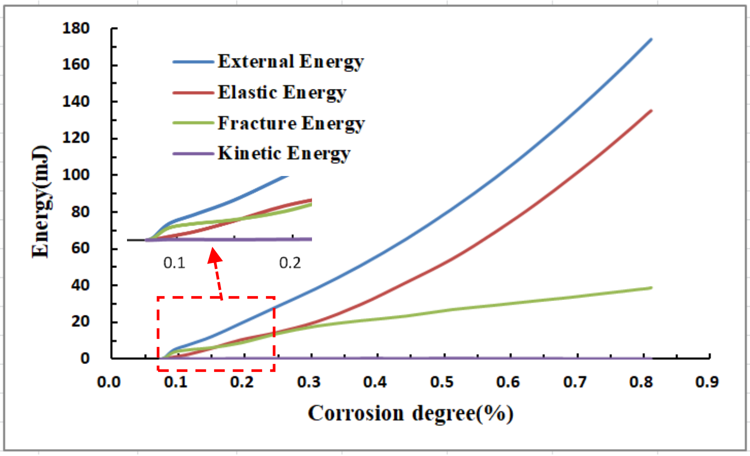

Figure 7 Energy evolutions as a function of corrosion degree.

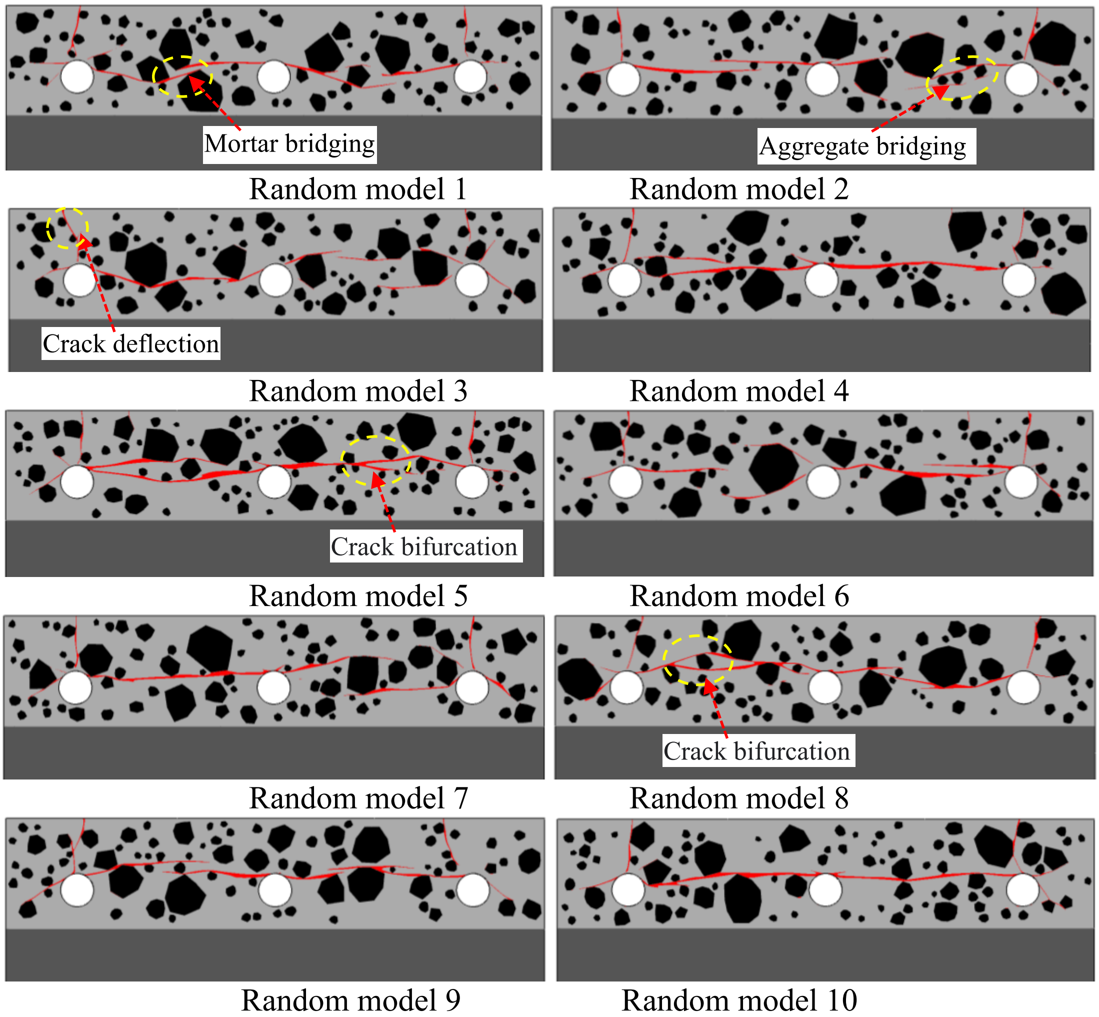

Figure 8 Crack patterns of 10 random meso-scale models.

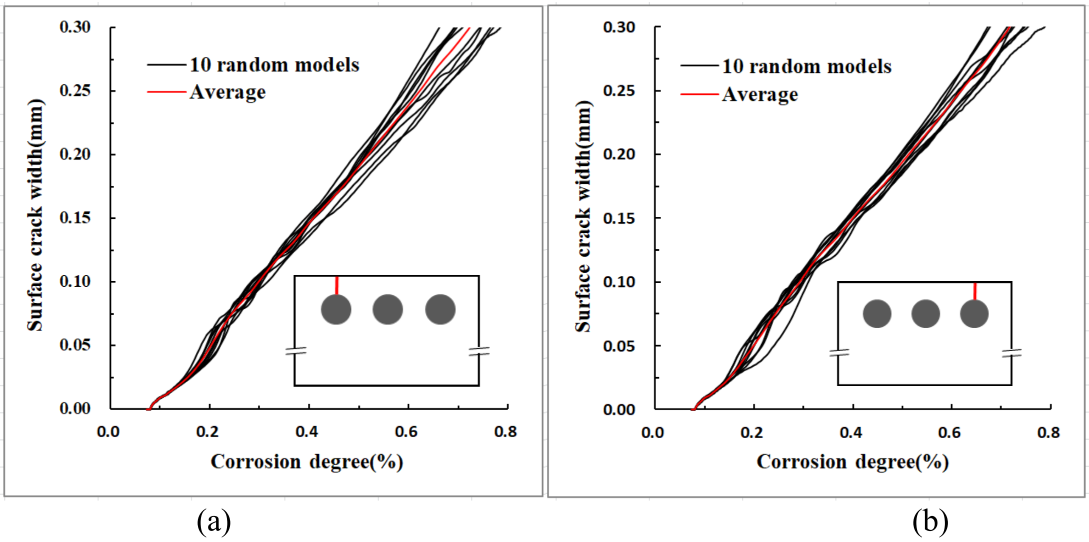

Figure 9 Crack width as a function of corrosion expansion displacement for 10 random models: (a) left top surface (b) right top surface.

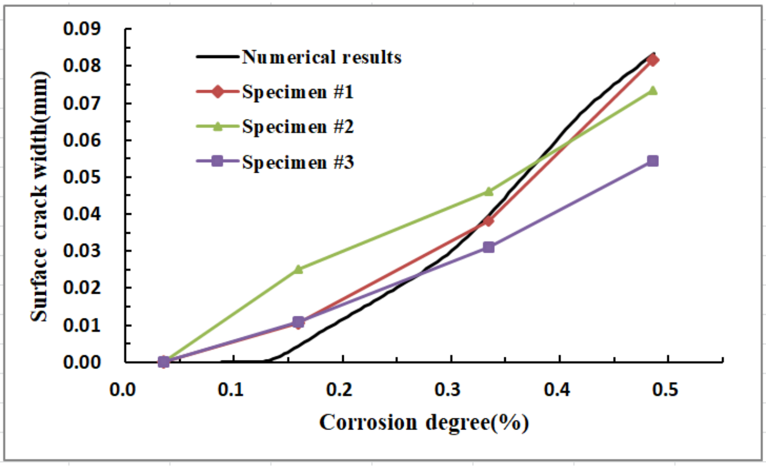

Figure 10 Comparison of surface crack width from numerical and experimental results [38]. The differences at the initial stage may be caused by the measurement error from a binocular lens with a precision of 0.01 mm.

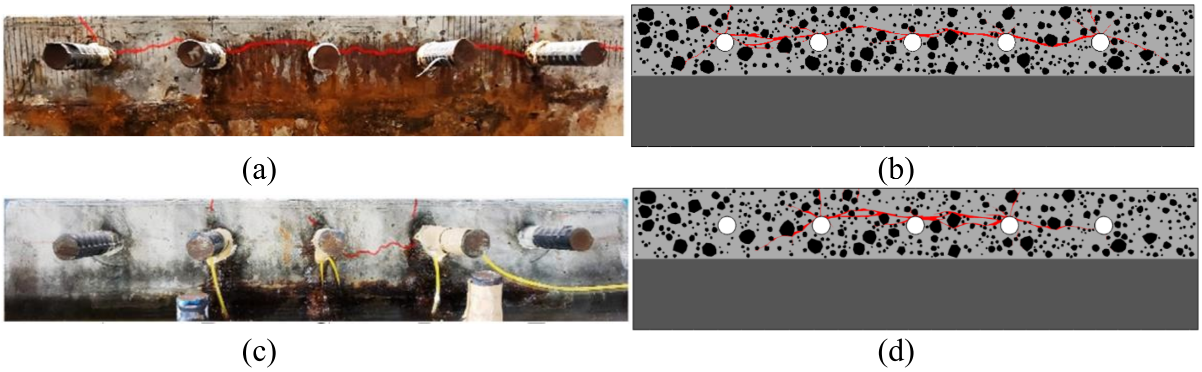

Figure 11 Comparison of crack patterns from numerical and experimental results [49]. (a) and (b) show the experimental and numerical results for all five reinforcement corrosion, respectively. (c) and (d) show the experimental and numerical results for the middle three reinforcement corrosion.

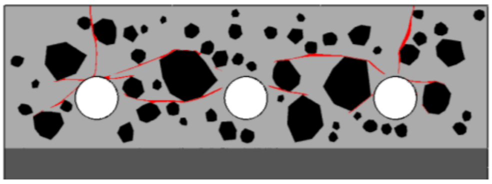

(a)

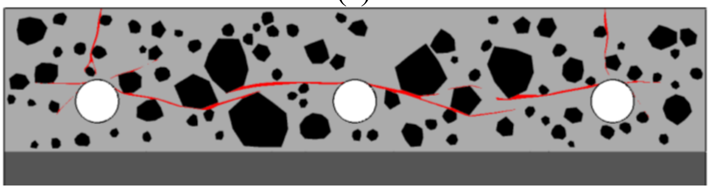

(b)

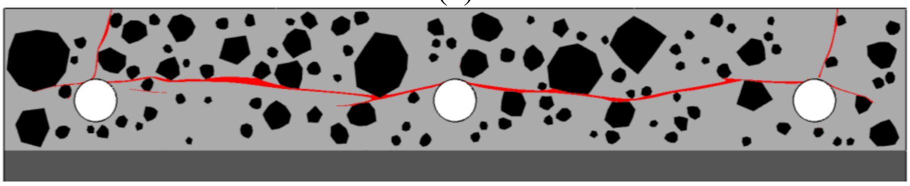

(c)

Figure 12 Crack patterns for different clearing spaces of reinforcements: (a) 30 mm; (b) 60 mm; (c) 90 mm.

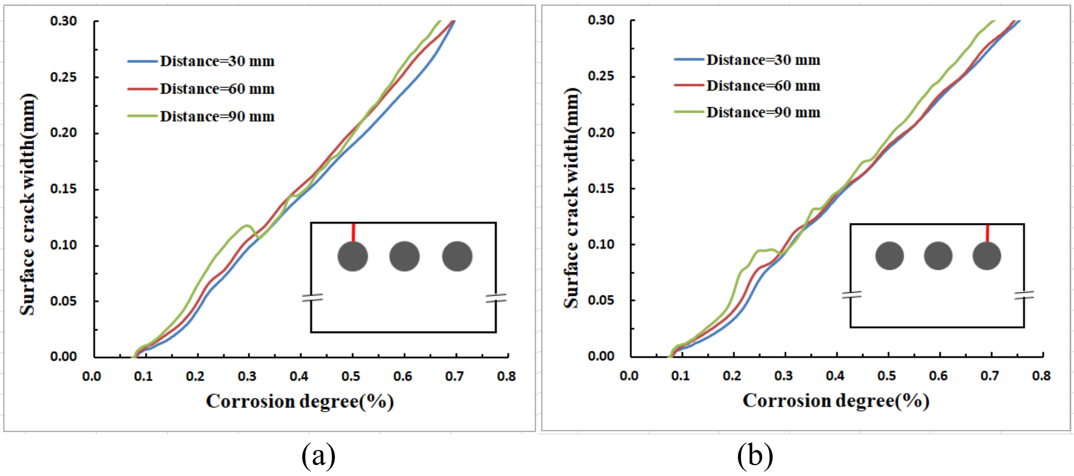

Figure 13 The crack width developments affected by the clear spacing of reinforcement: (a) left top surface (b) right top surface. A sudden drop of top surface crack width occurs when a through crack forms for the clear spacing 90 mm.

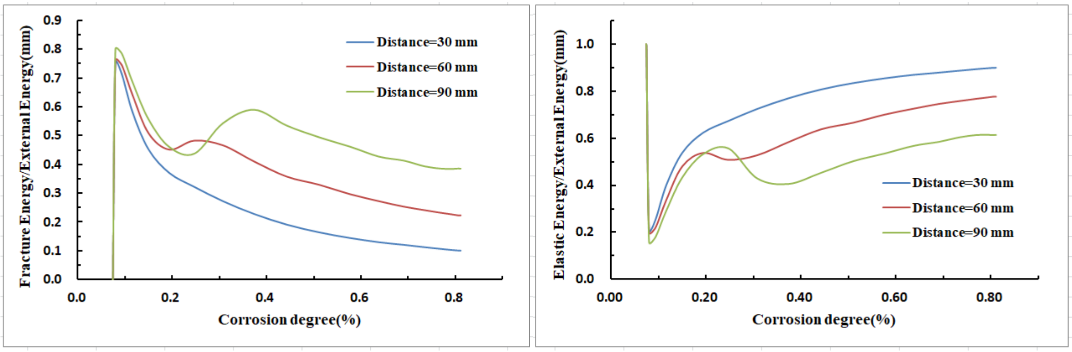

(a) (b)

Figure 14 The energy ratio developments for different reinforcement spacing: (a) fracture energy to external energy; (b) elastic energy to external energy. More external energy caused by corrosion is transferred to elastic energy for the RC structures with a smaller reinforcement clearing space.

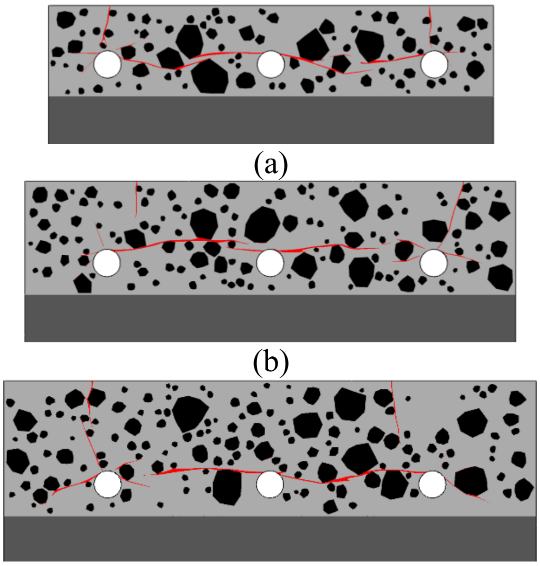

(a)

(b)

(c)

Figure 15 Crack patterns for different thicknesses of concrete cover: (a) 20 mm; (b) 30 mm; (c) 40 mm.

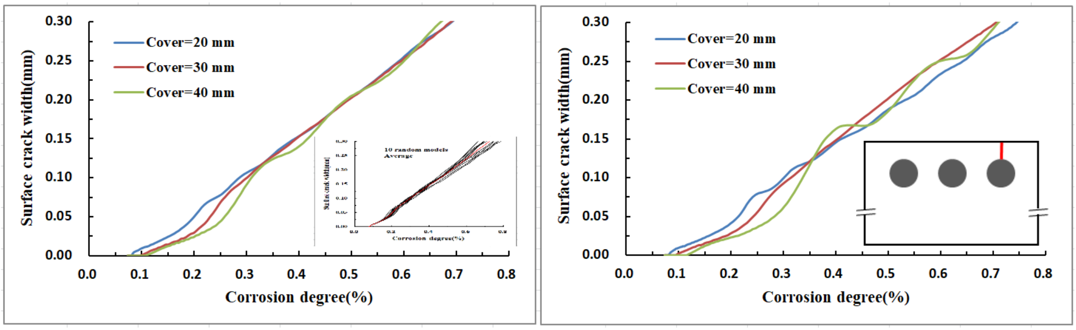

(a) (b)

Figure 16 The crack width developments for different thicknesses of concrete cover: (a) left top surface (b) right top surface.

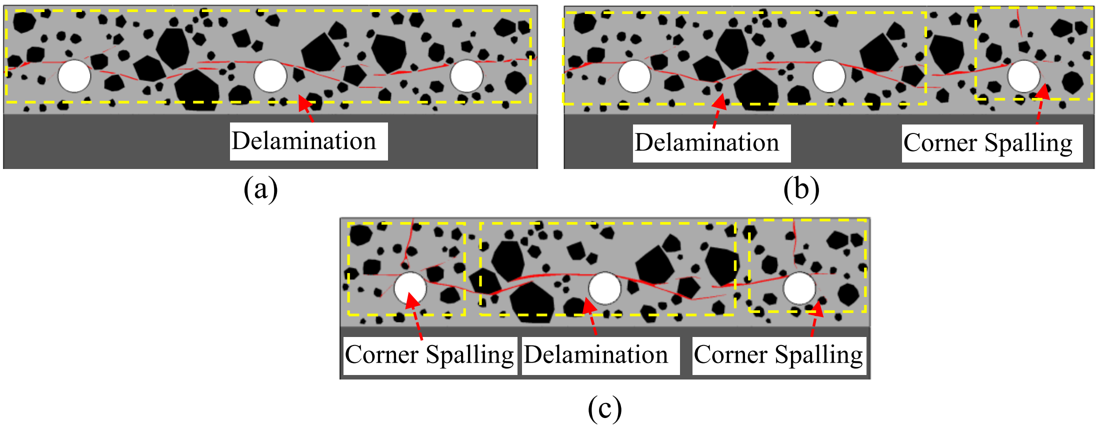

Figure 17 Crack patterns for different strengths of ITZ: (a) 0.1 MPa; (b) 0.25 MPa; (c) 1 MPa.

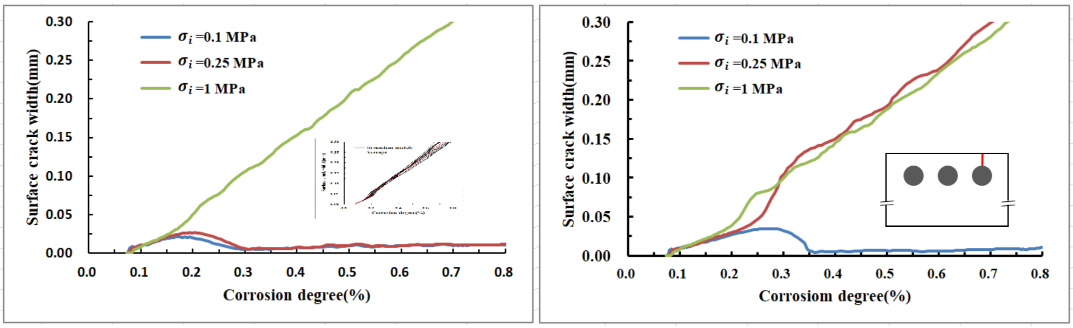

Figure 18 The crack width developments for different strengths of ITZ: (a) left top surface (b) right top surface.

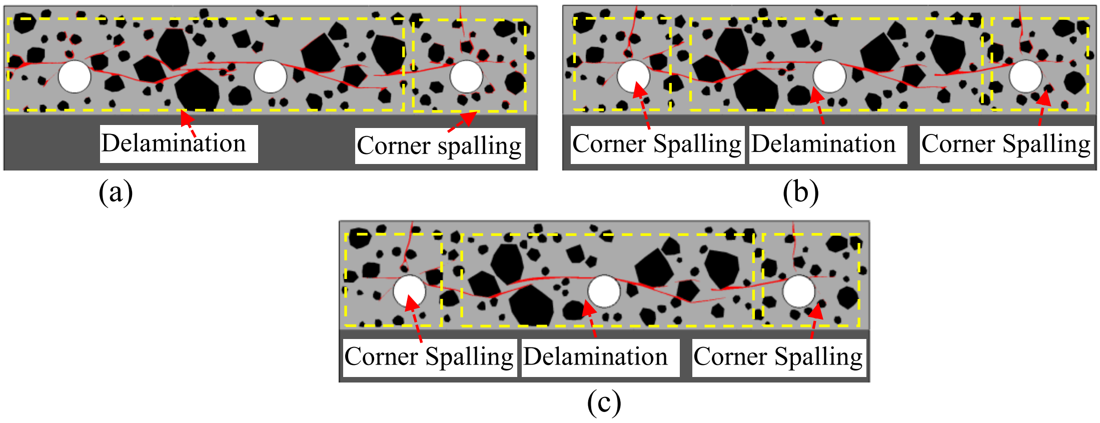

Figure 19 Crack patterns of concrete for different fracture energies of ITZ: (a) 0.00525 N/mm (b) 0.0105 N/mm; (c) 0.021 N/mm.

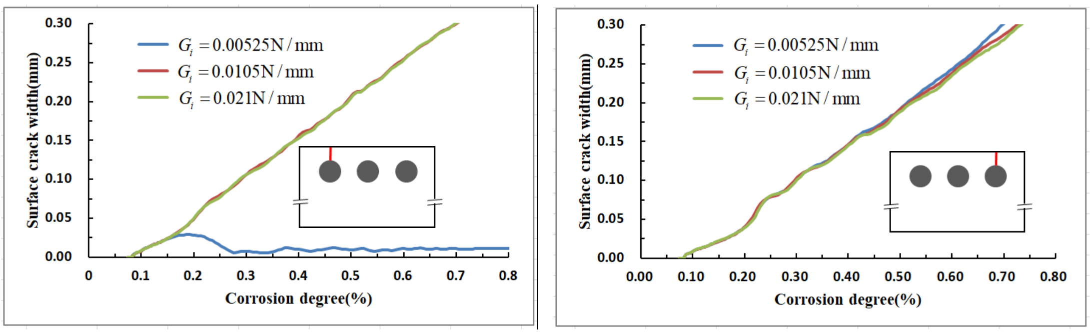

Figure 20 The crack width developments for different fracture energies of ITZ: (a) left top surface (b) right top surface.

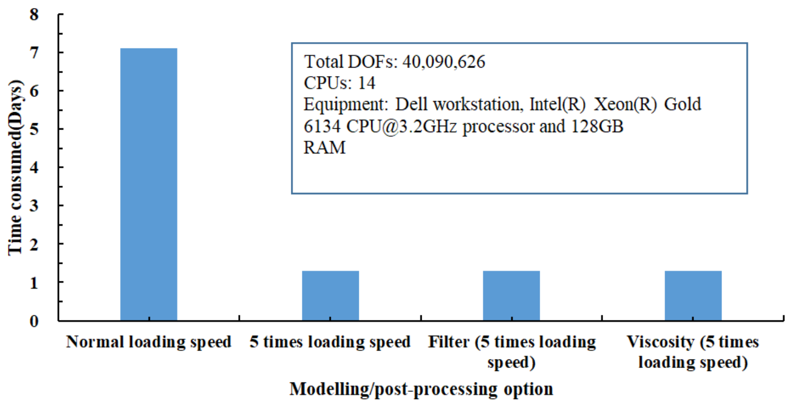

(a)

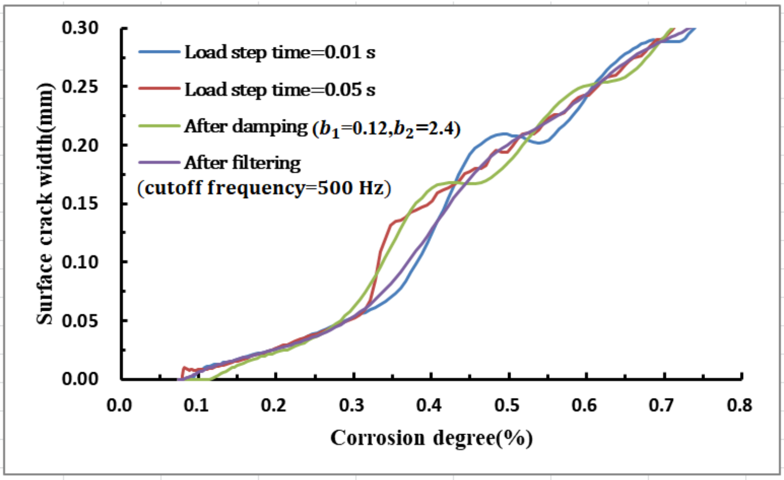

(b)

Figure 21 Expensed time (a) and the modelling results (b) with different modelling approaches.